Supplementary Information (SI) for Inorganic Chemistry Frontiers.
This journal is © the Partner Organisations 2025

Supporting information

Coordination-Induced In-Situ Confinement of Small-Sized Ag Nanoparticles on Ultrathin C_3N_4 with Strong Metal-Support Interaction for Enhanced Selective CO_2 Photoreduction

Qin Zhang,[a] Jiancong Liu,*[a] Dongxu Wang,[a] Chengxu Jin,[a] Li Fang,[a] Xingyu Li,[a] Yingjie Jiang,[a] Xin Wang,[a] Chungui Tian*[a]

[a]*Key Laboratory of Functional Inorganic Material Chemistry, Ministry of Education of the People's Republic of China, Heilongjiang University. Harbin 150080, China*

E-mail: jiancong@gmail.com, liujiancong@hlju.edu.cn, tianchungui@hlju.edu.cn, chunguitianhq@163.com.;

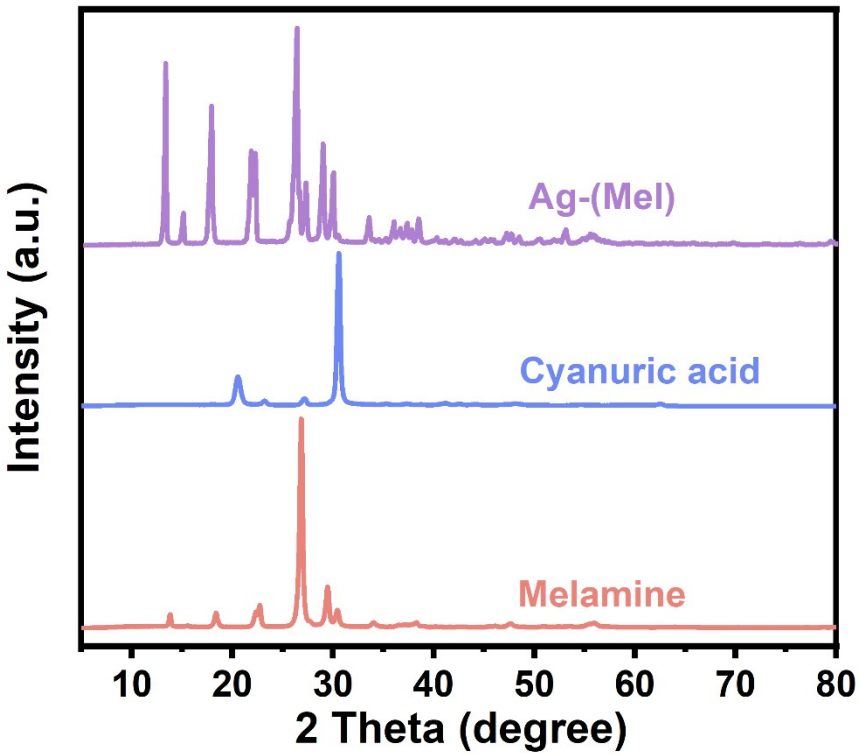

Figure S1. XRD pattern of melamine, cyanuric acid and Ag-(Mel).

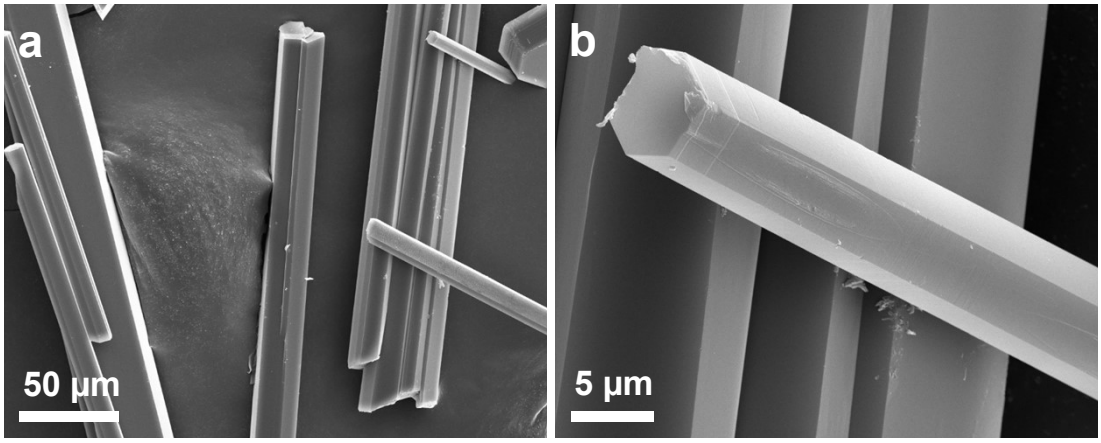

Figure S2. SEM images of supramolecular precursor.

The SEM images confirm that the synthesized supramolecular precursor material exhibits a typical hexagonal prismatic morphology.

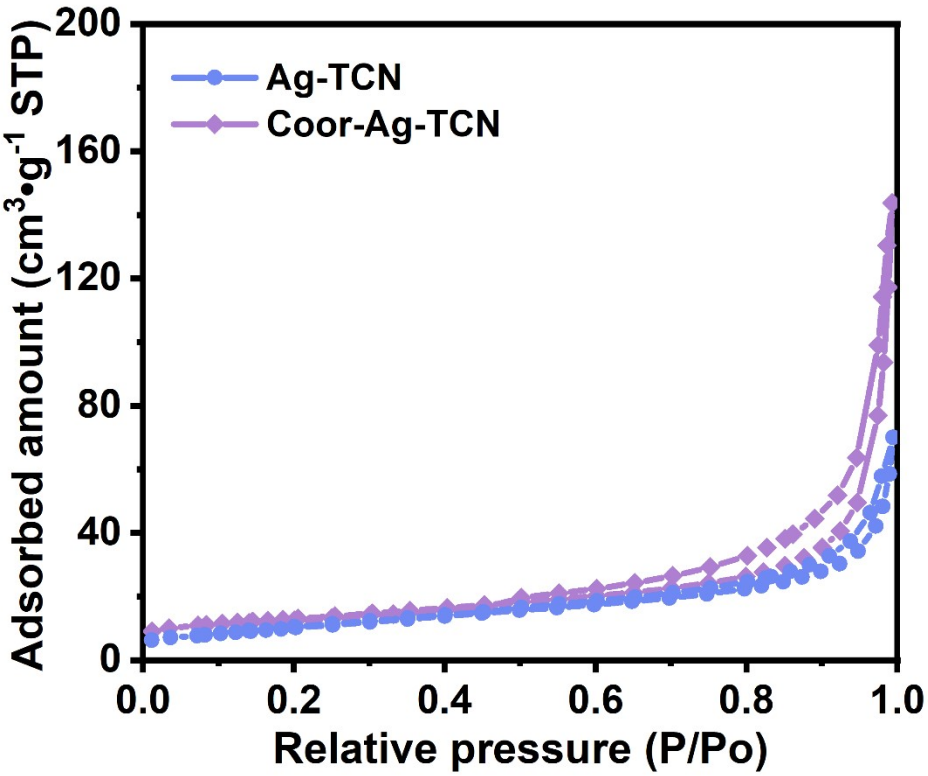

Figure S3. Nitrogen adsorption/desorption isotherms.

Nitrogen adsorption-desorption studies (Figure S3) demonstrate that Ag-TCN and Coor-Ag-TCN all exhibit type IV isotherms, verifying the well-defined hierarchical porous structure of the hollow tubular C_3N_4.

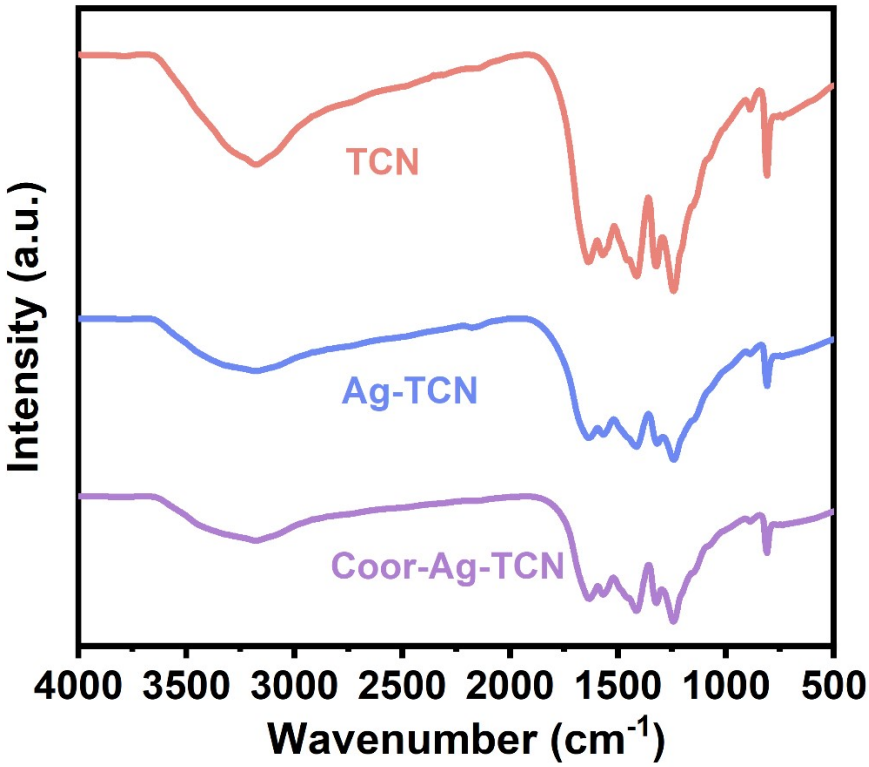

Figure S4. FT-IR spectra of the synthesized TCN, Ag-TCN and Coor-Ag-TCN.

The broad peak at 2900~3200 cm^{-1} is attributable to the N-H and O-H bands, which are caused by the residual amino groups and absorbed H_2O molecules, respectively. The absorption band ranging from 1200 to 1600 cm^{-1} is the characteristic vibration signal of the aromatic CN heterocycles.

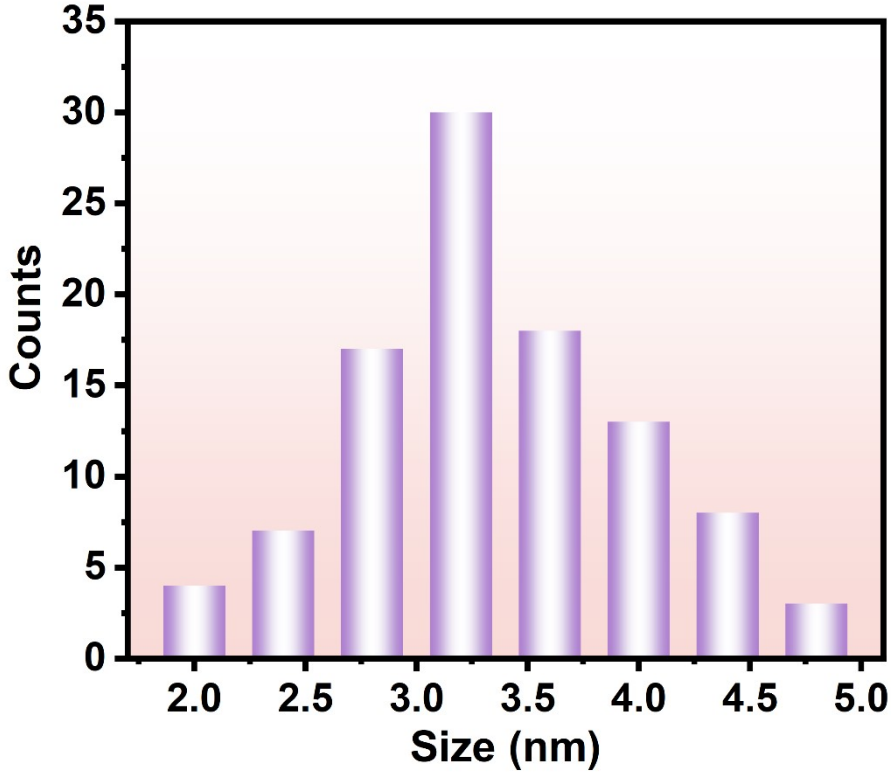

Figure S5. Size distribution of Ag NPs on the TCN.

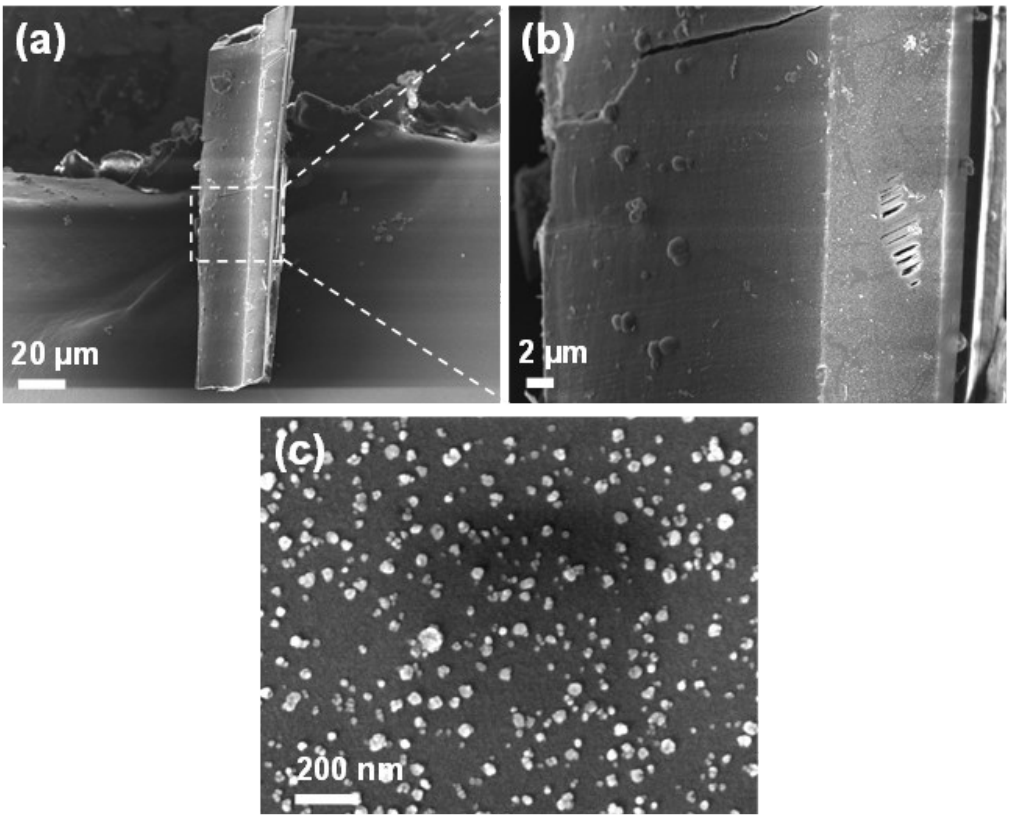

Figure S6. SEM images of Ag-TCN.

Through comparative studies, it was observed that when Ag nanoparticles were deposited onto C_3N_4 using direct photocatalysis, the resulting nanoparticles exhibited larger sizes and significant agglomeration.

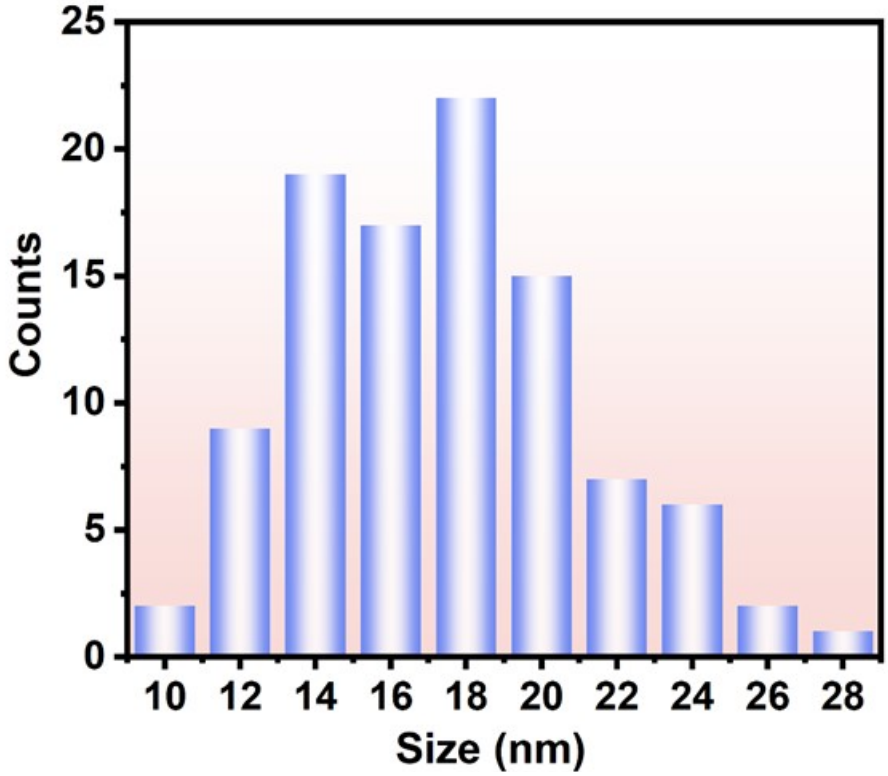

Figure S7. Diameter distribution of photo deposited silver particles.

The SEM images show the distribution of Ag nanoparticles on the C_3N_4 support. Accurate measurements show that the diameter of the silver nanoparticles is about 17.5 nm. The large nanoparticle size is not conducive to efficient charge transfer between the metal and the support.

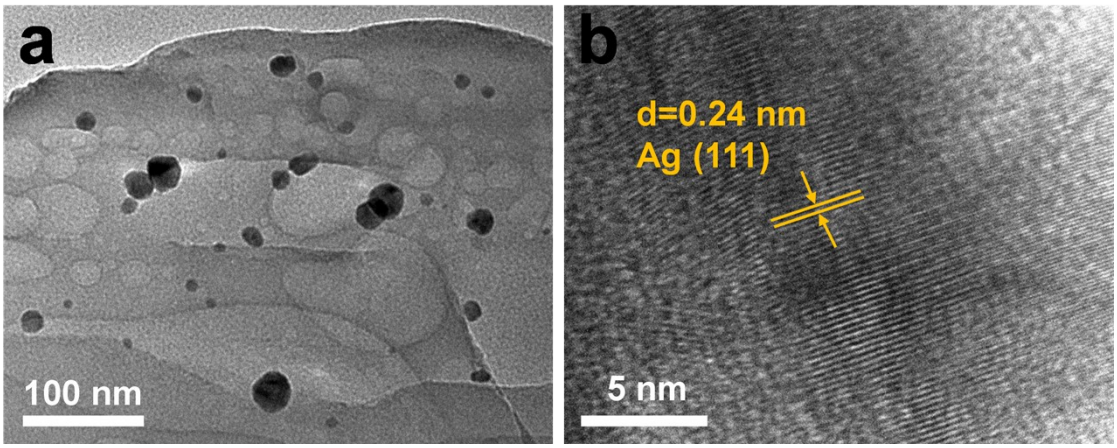

Figure S8. HR-TEM image of Ag-TCN.

High-resolution TEM images offer a critical microscopic perspective for investigating the crystal structure of silver nanoparticles. Analysis of high-resolution TEM images of individual Ag nanoparticles reveals a d-spacing of 0.24 nm, which corresponds to the (111) planes of silver.

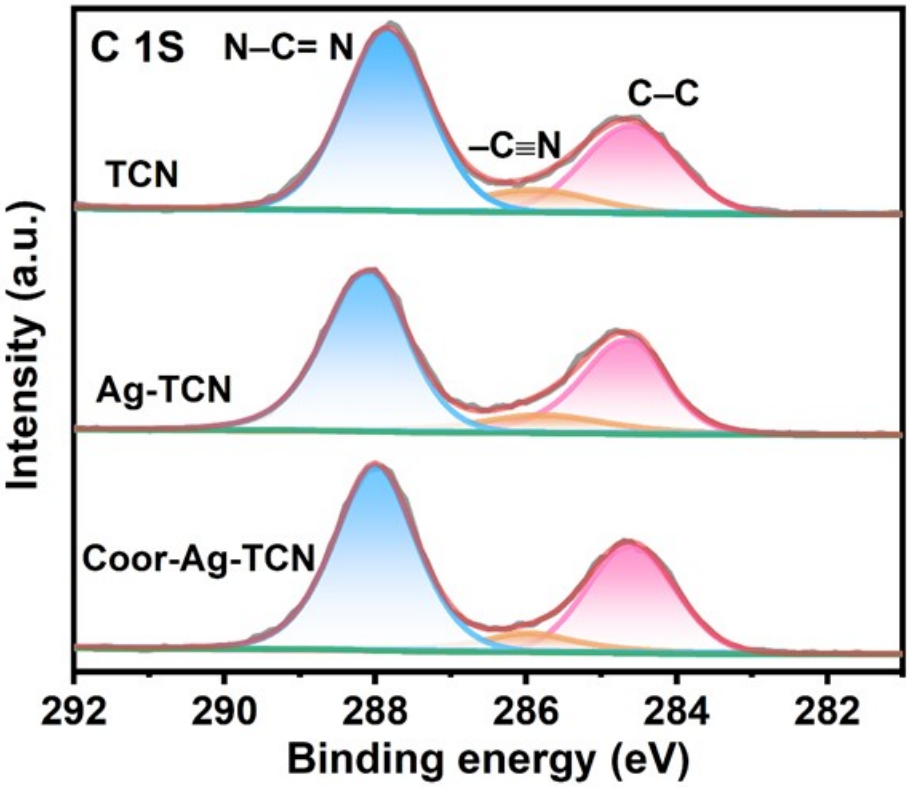

Figure S9. XPS C 1s spectra of TCN, Ag-TCN and Coor-Ag-TCN.

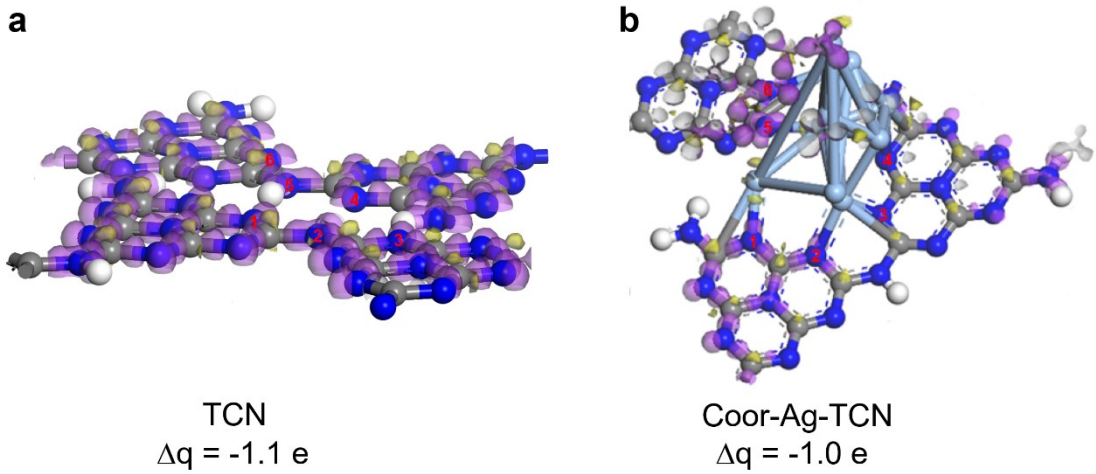

Figure S10. Differential charge densities of TCN and Coor-Ag-TCN (the charge depletion and accumulation in space are respectively in yellow and violet).

Figure S11. An automated online micro-gas chromatograph for photocatalytic CO_2 reduction.

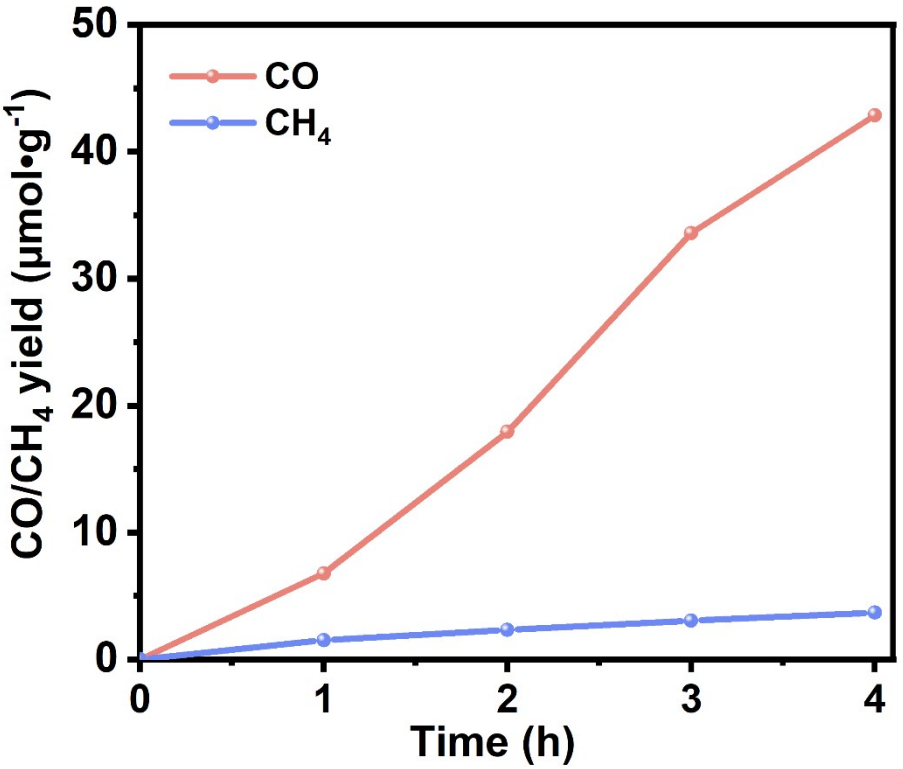

Figure S12. The yields of CO and CH_4 over Ag NPs.

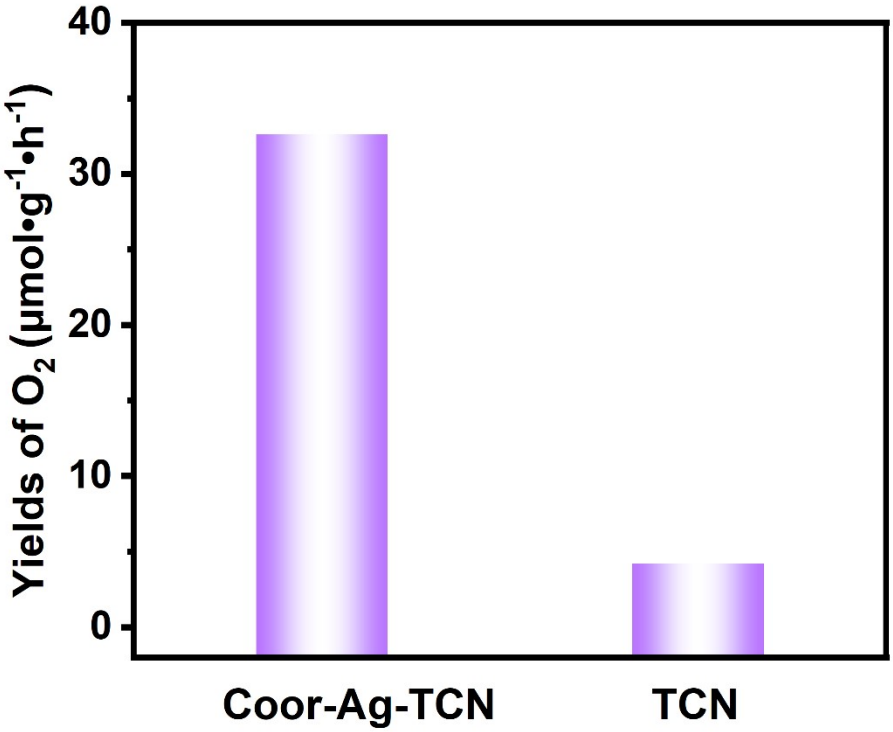

Figure S13. The Yields of O_2 over Coor-Ag-TCN and TCN.

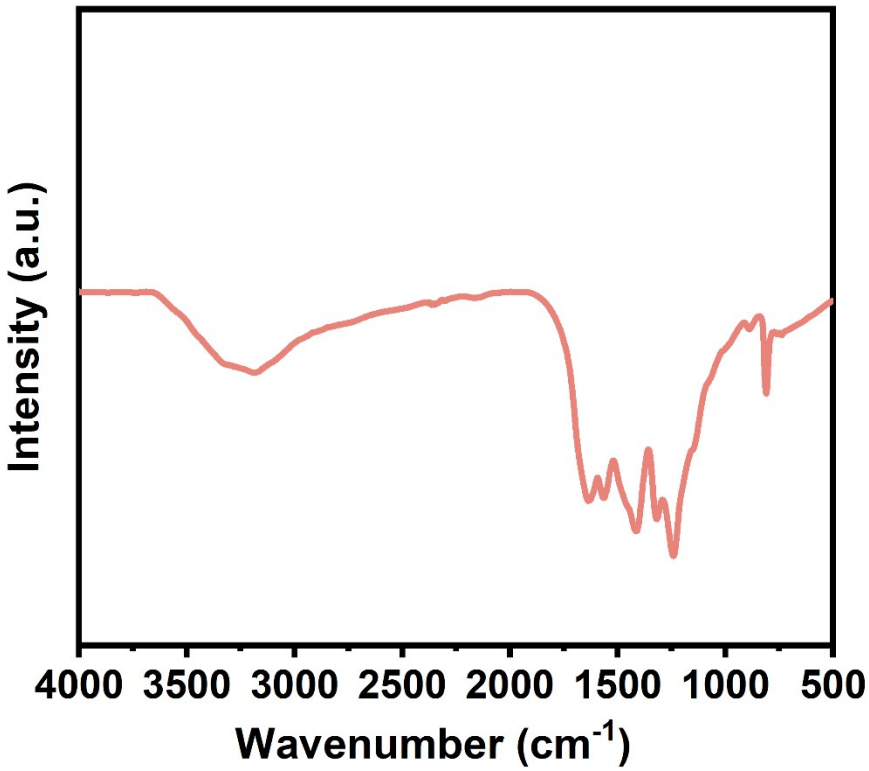

Figure S14. FT-IR spectra of Coor-Ag-TCN after the photocatalytic reaction.

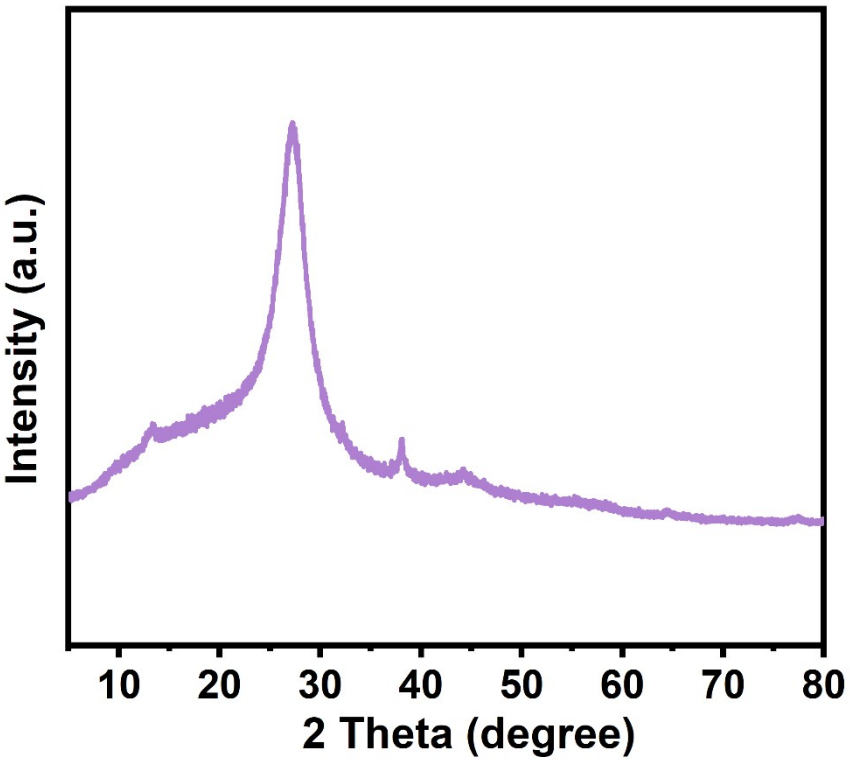

Figure S15. XRD spectra of Coor-Ag-TCN after the photocatalytic reaction.

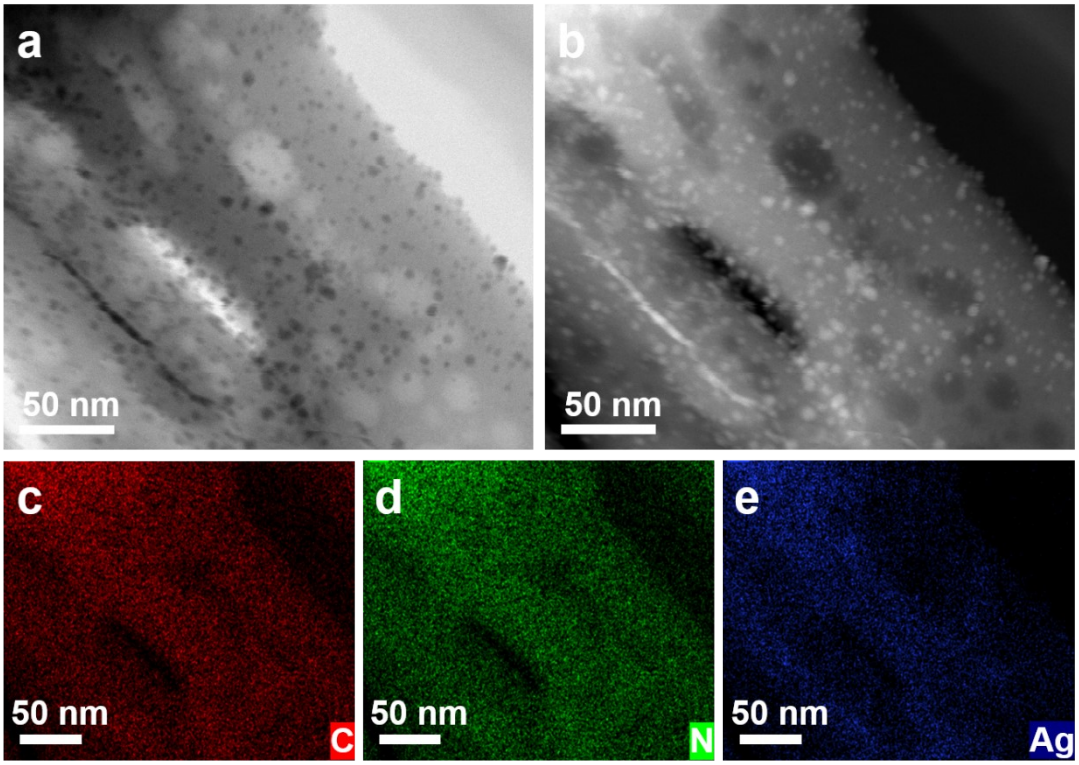

Figure S16. (a) TEM image and (b-e) the corresponding elemental mapping images of Coor-Ag-TCN after the photocatalytic reaction.

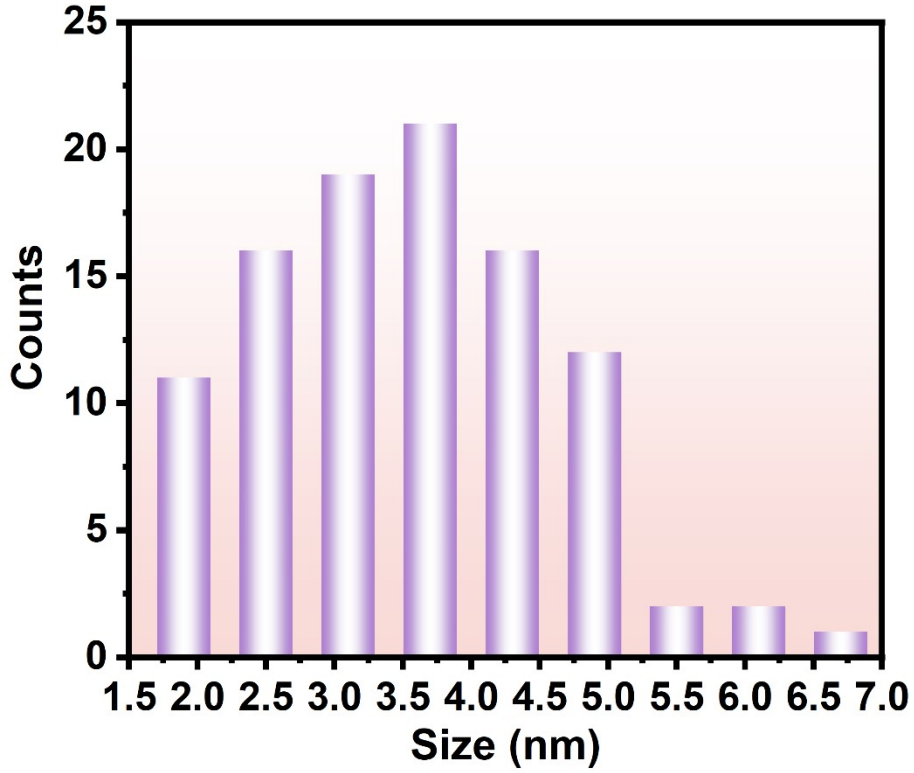

Figure S17. Diameter distribution of photo deposited Ag NPs of Coor-Ag-TCN after the photocatalytic reaction.

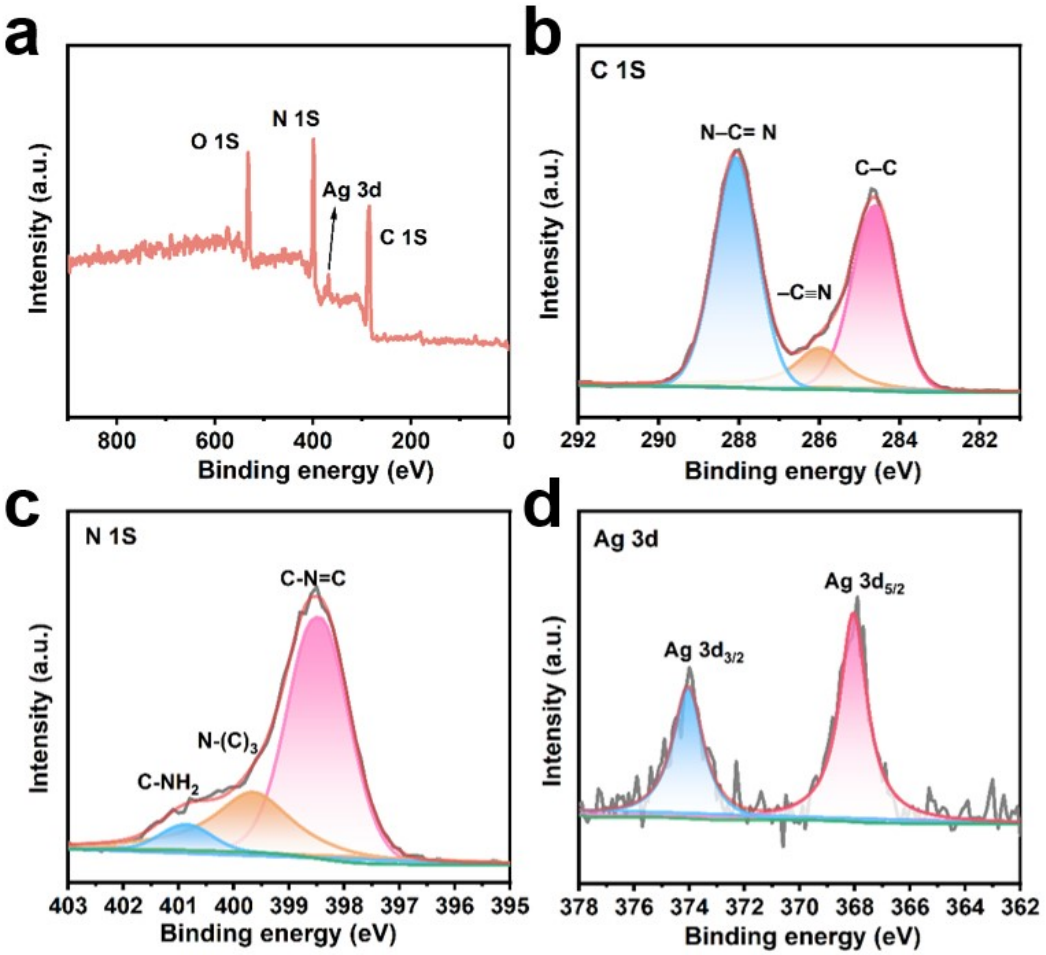

Figure S18. (a) The XPS survey spectra, (b) C 1S, (c) N 1S, (d) Ag 3d spectra of Coor-Ag-TCN after photocatalytic reaction.

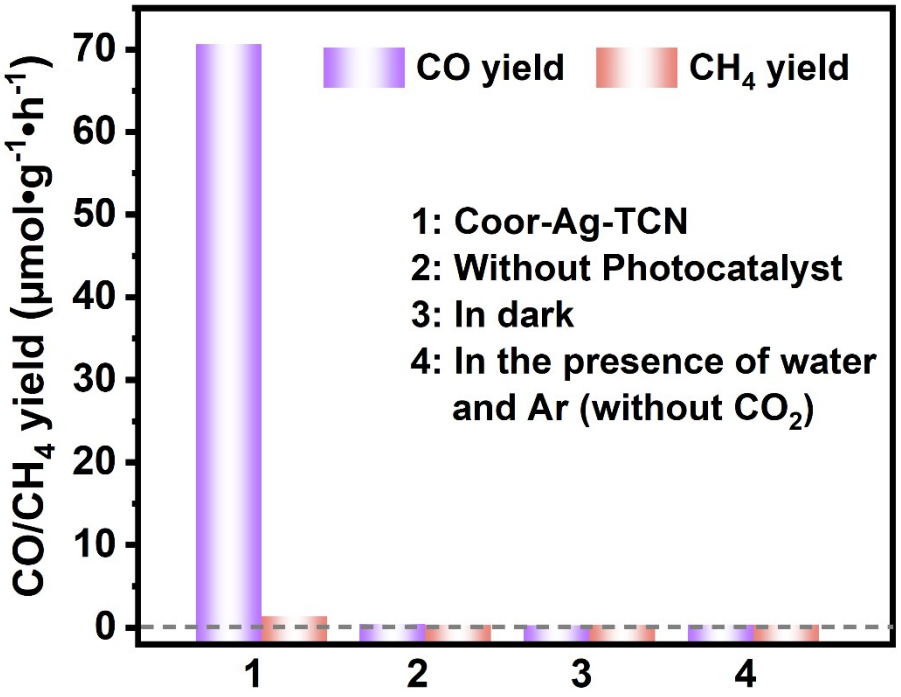

Figure S19. Yields of CO and CH_4 on Coor-Ag-TCN under different reactive conditions.

Table S1. The Ag content of Ag-TCN, Coor-Ag-TCN and Coor-Ag-TCN spent.

Samples	Ag (mas.%) from ICP-OES
Ag-TCN	1.23
Coor-Ag-TCN	1.30
Coor-Ag-TCN spent	1.28

The silver content in the sample was determined to be 1.30 wt% using inductively coupled plasma atomic emission spectrometry (ICP-AES), whereas the Ag content in the reference sample was measured at 1.23%.

Table S2. XPS peak area ratio of samples.

Samples	C-N=C	$N-(C)_3$	N-CH	$C-N=C/N-(C)_3$
TCN	67.4	21.6	11.0	3.13
Ag-TCN	68.1	25.1	6.8	2.72
Coor-Ag-TCN	68.3	27.7	4.00	2.46
Coor-Ag-TCN spent	65.1	28.7	6.2	2.27

Table S3. Elemental analysis data of TCN and Coor-Ag-TCN.

Samples	Mole Percentage / %			Atomic Ratio (C/N)
	N	C	H	
TCN	45.26	30.30	24.44	0.67
Coor-Ag-TCN	42.56	29.90	27.54	0.70

Table S4. Kinetic parameters derived from the Time-resolved PL decay spectra.

Samples	t_1 (ns)	A_1	t_2 (ns)	A_2	t_{ave} (ns)
TCN	17.1252	0.35914	2.97479	39.70176	3.67
Coor-Ag-TCN	4.31309	12.31739	23.71436	0.26489	6.36

Table S5. Product yield and CO selectivity of samples.

Samples	CO (umolg$\cdot^{-1}h^{-1}$)	CH_4 (umolg$\cdot^{-1}h^{-1}$)	Selectivity (%)
TCN	12.78	1.05	92.41
Ag-TCN	22.90	1.48	93.93
Coor-Ag-TCN	70.63	1.35	98.12

Table S6. Comparison photocatalytic CO_2 conversion performance with previously reported g-C_3N_4 based photocatalysts.

Photocatalyst	Light sources	CO evolution rate (umol·g^{-1}h^{-1})	Product Selectivity (%)	Reaction condition	Ref
Coor-Ag-TCN	300 W Xe lamp with an AM1.5 filter	70.63	98.12	CO_2+H_2O	This Work
Cu_1/N_{2C}V-CN	300 W Xe lamp with an AM1.5 filter	11.12	98.5	CO_2+H_2O	[1]
Cu cluster/CN	300 W Xe lamp (λ≥420 nm)	5.0	90.4	10%TEOA+CO_2+H_2O	[2]
Cu_1N_3@ PCN-1	300 W Xe lamp (λ≥420 nm)	49.8	>99%	CO_2+H_2O	[3]
30% InVO-CN	300 W Xe lamp (λ≥420 nm)	20.14	_	CO_2+H_2O	[4]
α-Fe_2O_3/BCN	300 W Xe lamp with an AM1.5 filter	11.02	_	CO_2+H_2O	[5]
β-In_2S_3/NDCN	300 W Xe lamp (λ≥420 nm)	20.32	_	CO_2+H_2O	[6]
PtCu-crCN	300 W Xe lamp with an AM1.5 filter	11.74	_	CO_2+H_2O	[7]
Mn_1Co_1/CN	300 W Xe lamp (λ≥420 nm)	47	_	CO_2+H_2O	[8]
CCN-W	300 W Xe lamp	11.91	_	CO_2+H_2O	[9]
Ni-CN-Ar-2	300 W Xe lamp	19.85	_	CO_2+H_2O	[10]
$Co_1Ag_{(n+1)}$-PCN	300 W Xe lamp	11.7	70.1	CO_2+H_2O +CH_3CN	[11]
Bi_2WO_6-C_3N_4	300 W Xe lamp with an AM1.5 filter	25.54	_	CO_2+H_2O	[12]
Ag-g-C_3N_4/BN-C	300 W Xe lamp (λ≥420 nm)	33.3	_	CO_2+H_2O	[13]
TNPs@CN	300 W Xe lamp with wavelength ranging from 320 to 780 nm.	26.89	_	CO_2+H_2O	[14]

References

1. Y. Duan, Y. Wang, W. Zhang, J. Zhang, C. Ban, D. Yu, K. Zhou, J. Tang, X. Zhang, X. Han, L. Gan, X. Tao and X. Zhou, Simultaneous CO_2 and H_2O Activation via Integrated Cu Single Atom and N Vacancy Dual-Site for Enhanced CO Photo-Production, *Adv. Funct. Mater.*, 2023, **33**, 2301729.
2. X. Zhang, X. Ran Zhang, P. Yang, H.-S. Chen and S. Ping Jiang, Black magnetic Cu-g-C_3N_4 nanosheets towards efficient photocatalytic H_2 generation and CO_2/benzene conversion, *Chem. Eng. J.*, 2022, **450**, 138030.
3. X. Sun, L. Sun, G. Li, Y. Tuo, C. Ye, J. Yang, J. Low, X. Yu, J. H. Bitter, Y. Lei, D. Wang and Y. Li, Phosphorus Tailors the d-Band Center of Copper Atomic Sites for Efficient CO_2 Photoreduction under Visible-Light Irradiation, *Angew. Chem. Int. Ed.*, 2022, **61**, e202207677.
4. M. Yu, J. Wang, G. Li, S. Zhang and Q. Zhong, Construction of 3D/2D indium vanadate/graphite carbon nitride with nitrogen defects Z-scheme heterojunction for improving photocatalytic carbon dioxide reduction, *J Mater Sci Technol*, 2023, **154**, 129-139.
5. X. Wang, F. Liang, H. Gu, S. Wu, Y. Cao, G. Lv, H. Zhang, Q. Jia and S. Zhang, In situ synthesized α-Fe_2O_3/BCN heterojunction for promoting photocatalytic CO_2 reduction performance, *J. Colloid Interface Sci.*, 2022, **621**, 311-320.
6. J. Wang, Y. Wang, M. Yu, G. Li, S. Zhang and Q. Zhong, Formation of flaky carbon nitride and beta-Indium sulfide heterojunction with efficient separation of charge carriers for enhanced photocatalytic carbon dioxide reduction, *J. Colloid Interface Sci.*, 2022, **611**, 71-81.
7. L. Cheng, P. Zhang, Q. Wen, J. Fan and Q. Xiang, Copper and platinum dual-single-atoms supported on crystalline graphitic carbon nitride for enhanced photocatalytic CO_2 reduction, *Chin. J. Catal.*, 2022, **43**, 451-460.
8. H. Ou, S. Ning, P. Zhu, S. Chen, A. Han, Q. Kang, Z. Hu, J. Ye, D. Wang and Y. Li, Carbon Nitride Photocatalysts with Integrated Oxidation and Reduction Atomic Active Centers for Improved CO_2 Conversion, *Angew. Chem. Int. Ed.*, 2022, **61**, e202206579.
9. Y. Liang, X. Wu, X. Liu, C. Li and S. Liu, Recovering solar fuels from photocatalytic CO_2 reduction over W^{6+}-incorporated crystalline g-C_3N_4 nanorods by synergetic modulation of active centers, *Appl.Catal.B Environ.*, 2022, **304**, 120978.
10. L. Ma, R. Guan, W. Kang, Z. Sun, H. Li, Q. Li, Q. Shen, C. Chen, X. Liu, H. Jia and J. Xue, Preparation of highly dispersed Ni single-atom doped ultrathin g-C_3N_4 nanosheets by metal vapor exfoliation for efficient photocatalytic CO_2 reduction, *J. Colloid Interface Sci.*, 2024, **660**, 381-392.
11. A. Deng, E. Zhao, Q. Li, Y. Sun, Y. Liu, S. Yang, H. He, Y. Xu, W. Zhao, H. Song, Z. Xu and Z. Chen, Atomic Cobalt–Silver Dual-Metal Sites Confined on Carbon Nitride with Synergistic Ag Nanoparticles for Enhanced CO_2 Photoreduction, *ACS Nano*, 2023, **17**, 11869-11881.
12. Y. Liu, R. Zou, Z. Chen, W. Tu, R. Xia, E. I. Iwuoha and X. Peng, Engineering a Hydrophobic–Hydrophilic Diphase in a Bi_2WO_6–C_3N_4 Heterojunction for Solar-Powered CO_2 Reduction, *ACS Catal.*, 2024, **14**, 138-147.
13. Y. Li, Z. Liu, Z. Li and Q. Wang, Renewable biomass-derived carbon-supported g-C_3N_4 doped with Ag for enhanced photocatalytic reduction of CO_2, *J. Colloid Interface Sci.*, 2022, **606**, 1311-1321.
14. Z. Li, J. Xiong, Y. Huang, Y. Huang, G. I. N. Waterhouse, Z. Wang, Y. Mao, Z. Liang and X. Luo, Synergy mechanism of confined effect and Z-scheme electron transfer in core–shell structure photocatalyst for boosting photoreduction CO_2 activity, *Chem. Eng. J.*, 2024, **486**, 150304.